Effects of finite-size heavy particles on the turbulent flows in a square duct[*]

Zhao-wu Lin (林昭武)[1], Xue-ming Shao (邵雪明)[1], Zhao-sheng Yu (余钊圣)[1], Lian-ping Wang (王连平)[2]
1. *State Key Laboratory of Fluid Power and Mechatronic Systems, Department of Mechanics, Zhejiang University, Hangzhou 310027, China, E-mail: lin3030612023@163.com*
2. *Department of Mechanical Engineering, University of Delaware, Newark, Delaware 19716, USA*

Abstract: A parallel direct-forcing fictitious domain method is applied in fully-resolved numerical simulations of particle-laden turbulent flows in a square duct. The effects of finite-size heavy particles on the mean secondary flow, the mean streamwise velocity, the root-mean-square velocity fluctuation, and the particle concentration distribution are investigated at the friction Reynolds number of 150, the particle volume fraction of 2.36%, the particle diameter of 0.1 duct width, and the Shields number ranging from 1.0 to 0.2. Our results show that the particle sedimentation breaks the up-down symmetry of the mean secondary vortices, and results in a stronger secondary-flow circulation which transports the fluids downward in the bulk center region and upward along the side walls at a low Shields number. This circulation has a significant impact on the distribution of the mean streamwise velocity, whose maximum value occurs in the lower half duct, unlike in the plane channel case. The flow resistance is increased and the turbulence intensity is reduced, as the Shields number is decreased. The particles accumulate preferentially at the face center of the bottom wall, due to the effect of the mean secondary flow. It is observed that the collision model has an important effect on the results, but does not change the results qualitatively.

Key words: Turbulent duct flow, particle-laden flow, mean secondary flow, fictitious domain method

Introduction

The turbulent flow in a square duct is characterized by the presence of mean cross-stream fluid motions. This kind of secondary flows, induced by turbulence fluctuations, takes the form of eight symmetrical vortices, with two counter-rotating vortices in pairs in each quadrant of the duct (see Fig.2). The mean secondary flows transport the fluid momentum from the bulk region to the corner areas along each corner bisector, and then back to the bulk regions along the wall bisectors. The early experimental measurements of the turbulent flows in a square duct were focused on the Reynolds stresses as the source for the genera-

tion of mean secondary flows. Direct numerical simulations of the single-phase turbulent flow in a square duct were performed by Gavrilakis[1], Uhlmann et al.[2] and Pinelli et al.[3].

There are limited studies of the particle-laden turbulent flows in a square duct in the literature. Winkler et al.[4] investigated the preferential concentration of particles in a fully developed turbulent square duct flow, and observed that particles tended to accumulate in regions of high strain-rate and low swirling strength. Sharma and Phares[5] reported that the mean secondary flow enhanced the lateral mixing for passive tracers and low-inertia particles, and higher inertia particles accumulated close to the wall. Winkler et al.[6], Yao and Fairweather[7] and Yao et al.[8] investigated the particle deposition in turbulent square duct flows. The results of Winkler et al.[6] show that the deposition occurs with greater probability near the center of the duct walls than at the corners. On the other hand, Yao and Fairweather[7] and Yao et al.[8] concluded that high-inertia particles tend to deposit close to the corners of the duct floor, while low-inertia particles deposit near the floor center. Yao and Fairweather[9] investi-

gated the resuspension of inertial particles in a turbulent square duct flow and demonstrated the important role of the mean secondary flow in the resuspension process.

In these studies of two-phase flows, the point-particle approximation was employed to deal with the particle motion, which is valid in principle only when the particle size is smaller than the Kolmogorov length scale and the particle volume fraction is low. In recent years, the interface-resolved direct numerical simulation methods were used to study the mechanisms of the interactions between the turbulence and the finite-size particles, to determine the interface between a particle and the fluid and all turbulent structures with the direct numerical simulation method. Such methods were applied to simulations of particle-laden wall-bounded turbulent flows such as the pipe flow[10] and the horizontal channel flows[11-15]. We investigated the effects of the finite-size neutrally buoyant particles on the turbulent flows in a square duct with the interface-resolved DNS method, and observed that the particle addition increased the intensity of the mean secondary flow. In the present paper, we report our results on the particle effects on the turbulent duct flow when the particle sedimentation effect is present. It is noted that in the previous studies based on the point-particle approximation, the modulation of the turbulent duct flow by the particles has not been made clear.
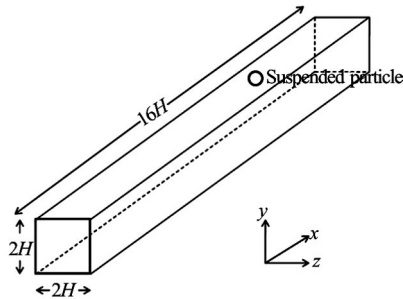

Fig.1 Geometrical model for the duct flow

1. Numerical model

1.1 Flow model

A schematic diagram of the geometrical model for the duct flow is shown in Fig.1. The x-axis is aligned in the streamwise direction. The z-axis direction is taken as the spanwise direction and y-axis direction as the transverse direction, as in the plane channel flow case. The corresponding velocity components in the (x,y,z) directions are $\boldsymbol{u}=(u,v,w)$, respectively. The no-slip velocity boundary condition is imposed at the duct walls and the periodic boundary condition is imposed in the streamwise direction. We denote the half width of the duct as H. In the present

study, the computational domain is $[0,16H]\times[-H,H]\times[-H,H]$.

We take H as the characteristic length and the friction velocity u_τ as the characteristic velocity in the non-dimensionalized scheme. The friction velocity is defined as $u_\tau=\sqrt{\tau_w/\rho_f}$, with τ_w being the mean shear stress on all walls, and ρ_f the fluid density. Thus, the Reynolds number is defined as $Re_\tau = u_\tau H/\nu$, with ν being the fluid kinematic viscosity. The pressure gradient is kept constant in our simulations, as $(-\mathrm{d}p/\mathrm{d}x)^e = 2\tau_w/H$, and its dimensionless value normalized by $\rho_f u_\tau^2/H$ is 2.

1.2 Direct-forcing fictitious domain method

A parallel direct-forcing fictitious domain method (DF/FD) is employed for the simulation of particle-laden turbulent duct flows. The fictitious domain (FD) method for the particulate flows was originally proposed by Glowinski et al.[16]. The key idea of this method is that the interior of the particles is filled with the fluids and the inner fictitious fluids are enforced to satisfy the rigid body motion constraint through a pseudo body force, introduced as a distributed Lagrange multiplier in the FD formulation[16]. In what follows, we describe the DF/FD method briefly, and the details can be found in Yu and Shao[17].

For simplicity of description, we will consider only one spherical particle in the following exposition. The particle density, volume and moment of inertia, the translational velocity, the angular velocity and the position are denoted by ρ_s, V_p, J, $\boldsymbol{U}$, $\boldsymbol{\omega}_p$ and $\boldsymbol{X}_p$, respectively. Let $P(t)$ represent the solid domain and Ω the entire domain including the interior and the exterior of the solid body. By introducing the following scales for the non-dimensionalization: H for length, u_τ for velocity, H/u_τ for time, $\rho_f u_\tau^2$ for the pressure, and $\rho_f u_\tau^2/H$ for the pseudo body force, the dimensionless FD formulation for the incompressible fluids and the spherical particles can be written as follows:

$$\frac{\partial \boldsymbol{u}}{\partial t} + \boldsymbol{u}\cdot\nabla\boldsymbol{u} = \frac{\nabla^2\boldsymbol{u}}{Re_\tau} - \nabla p + 2 + \lambda \quad \text{in} \quad \Omega \tag{1}$$

$$\boldsymbol{u} = \boldsymbol{U} + \boldsymbol{\omega}_s \times \boldsymbol{r} \quad \text{in} \quad P(t) \tag{2}$$

$$\nabla\cdot\boldsymbol{u} = 0 \quad \text{in} \quad \Omega \tag{3}$$

$$(\rho_r - 1)V_p^*\left(\frac{\mathrm{d}\boldsymbol{U}}{\mathrm{d}t} - Fr\frac{\boldsymbol{g}}{g}\right) = -\int_P \lambda \mathrm{d}\boldsymbol{x} \tag{4}$$

$$(\rho_r - 1)J^* \frac{\mathrm{d}\omega_p}{\mathrm{d}t} = -\int_P r \times \lambda \mathrm{d}x \qquad (5)$$

In the above equations, u represents the fluid velocity, p the fluid pressure minus a constant pressure gradient of 2, λ the pseudo-body force defined in the solid domain $P(t)$, r the position vector with respect to the mass center of the particle, ρ_r the particle-fluid density ratio defined as $\rho_r = \rho_s / \rho_f$, Fr the Froude number defined here as $Fr = gH / u_\tau^2$, V_p^* the dimensionless particle volume defined as $V_p^* = V_p / H^3$, and J^* the dimensionless moment of inertia defined as $J^* = J / \rho_s H^5$.

A fractional-step time scheme is used to decouple the system (1)-(5) into the following two sub-problems.

Fluid sub-problem for u^* and p:

$$\frac{u^* - u^n}{\Delta t} - \frac{1}{2}\frac{\nabla^2 u^*}{Re_\tau} = -\nabla p + 2 -$$

$$\frac{1}{2}[3(u \cdot \nabla u)^n - (u \cdot \nabla u)^{n-1}] + \frac{1}{2}\frac{\nabla^2 u}{Re_\tau} + \lambda^n \qquad (6)$$

$$\nabla \cdot u^* = 0 \qquad (7)$$

A finite-difference-based projection method on a homogeneous half-staggered grid is used for the solution of the above fluid sub-problem. All spatial derivatives are discretized with the second-order central difference scheme.

Particle sub-problem for U^{n+1}, ω_p^{n+1}, λ^{n+1} and u^{n+1}:

$$\rho_r V_p^* \frac{U^{n+1}}{\Delta t} = (\rho_r - 1)V_p^*\left(\frac{U^n}{\Delta t} - Fr\frac{g}{g}\right) + \int_P \left(\frac{u^*}{\Delta t} - \lambda^n\right)\mathrm{d}x \qquad (8)$$

$$\rho_r \frac{J^* \omega_p^{n+1}}{\Delta t} = (\rho_r - 1)\frac{J^* \omega_p^n}{\Delta t} + \int_P r \times \left(\frac{u^*}{\Delta t} - \lambda^n\right)\mathrm{d}x \qquad (9)$$

Note that the above equations are reformulated so that all the right-hand side terms are known quantities and consequently the particle velocities U^{n+1} and ω_p^{n+1} are obtained without iteration. Then, λ^{n+1} defined at the Lagrangian nodes are determined from

$$\lambda^{n+1} = \frac{U^{n+1} + \omega_p^{n+1} \times r - u^*}{\Delta t} + \lambda^n \qquad (10)$$

Finally, the fluid velocities u^{n+1} at the Eulerian nodes are corrected from

$$u^{n+1} = u^* + \Delta t(\lambda^{n+1} - \lambda^n) \qquad (11)$$

In the above manipulations, the tri-linear function is used to transfer the fluid velocity from the Eulerian nodes to the Lagrangian nodes, and the pseudo body force from the Lagrangian nodes to the Eulerian nodes.

We note that we have extended the fictitious domain method to simulate the fluid-structure interactions[18,19].

1.3 Collision model

The collision model is required to prevent the mutual penetration of particles and the penetration of particles into walls. Two soft-sphere collision models are adopted in the present study. One is the following artificial repulsive force collision model (referred to as ARF)

$$F = F_0\left(1 - \frac{d}{d_c}\right)n \qquad (12)$$

where F, d and n are the repulsive force, the gap distance and the unit normal vector between the particles i and j, respectively. d_c represents a cut-off distance and the repulsive force is activated at $d < d_c$. F_0 is the magnitude of the force at contact. We set $d_c = h$ (with h being the fluid mesh size), and $F_0 = 10^3$. The motions of the particles due to the collision force (12) and due to the hydrodynamic force (9)-(10) are handled separately with a fractional step scheme. The time step for the collision model is set to be one tenth of the latter (i.e., $\Delta t / 10$) to circumvent the stiffness problem due to the explicit integration scheme with a large value of F_0, as suggested by Glowinski et al.[16]. The collision between a particle and a wall is treated similarly as two particles with the coefficient F_0 in (12) doubled. This collision model was used by Shao et al.[11] for the simulations of particle-laden turbulent channel flows.

The other collision model adopted is the discrete element model (referred to as DEM) developed originally for the simulation of granular materials. In the DEM collision model, the mechanical elements such as a spring and a dash-dot are employed. Besides the spring-like repulsive force, the viscous damping force in the normal direction and the tangential friction force

are also considered. We adopt the model described in Crowe et al.[20]:

$$F_n = (-k_n \delta_n^{3/2} - \eta_n G \cdot n)n \qquad (13)$$

$$F_t = -k_t \delta_t - \eta_t G_{ct} \qquad (14)$$

where F_n, δ_n, k_n and η_n are the contact force on particle i, the overlap distance, the spring coefficient and the damping coefficient in the normal direction, respectively, and F_t, δ_t, k_t and η_t are the corresponding parameters in the tangential direction. Here n is the unit vector in the direction of the line from the center of particle i to that of particle j, and G is the velocity vector of particle i relative to particle j $(G = U_i - U_j)$. G_{ct} is the slip velocity given by

$$G_{ct} = G - (G \cdot n)n + a_i \omega_{pi} \times n + a_j \omega_{pj} \times n \qquad (15)$$

If the following relation is satisfied

$$|F_t| > f|F_n| \qquad (16)$$

particle i slides and the tangential force is given by the Coulomb-type friction law

$$F_t = -f|F_n|t \qquad (17)$$

where f is the friction coefficient and t is the unit vector of G_{ct}. In this study, we set the friction coefficient $f = 0.3$ for particles interacting with other particles and $f = 0.2$ for particles interacting with the walls.

The stiffness k_n of a sphere is expressed by using the Hertzian contact theory

$$k_n = \frac{4}{3}\left(\frac{1-\sigma_i^2}{E_i} + \frac{1-\sigma_j^2}{E_j}\right)^{-1}\left(\frac{r_i + r_j}{r_i r_j}\right)^{-1/2} \qquad (18)$$

where E and σ are the Young's modulus and the Poisson ratio, respectively. The stiffness k_t can be expressed by using the Mindlin's theory

$$k_t = 8\left(\frac{2-\sigma_i}{G_i} + \frac{2-\sigma_j}{G_j}\right)^{-1}\left(\frac{r_i + r_j}{r_i r_j}\right)^{-1/2}\delta_n^{1/2} \qquad (19)$$

where G is the particle shear modulus, which is related to the Young's modulus and the Poisson ratio, as follows

$$G = \frac{E}{2(1+\sigma)} \qquad (20)$$

The damping coefficients are given by

$$\eta_n = 2\sqrt{m_p k_n} \qquad (21)$$

$$\eta_t = 2\sqrt{m_p k_t} \qquad (22)$$

where m_p is the mass of the particle. We set $E = 3 \times 10^5$ and $\sigma = 0.33$. As pointed out by Crowe et al.[20], the elastic modulus adopted in the DEM simulation is normally less than the real value to avoid the excessively small time-step, and the results are not sensitive to the choice of the value, particularly for the particle collision in fluids. Unless otherwise specified, the results presented below are obtained with the DEM collision model.

1.4 *Parameter settings*

The friction Reynolds number Re_τ is 150, the particle volume fraction is $\phi = 2.36\%$, the particle-fluid density ratio is $\rho_r = 1.5$, and the particle radius a normalized by H is $a/H = 0.1$, throughout this study. Three different Shields numbers are considered: $\theta = 0.2, 0.5$ and 1.0. The Shields number reflects the relative importance of the shear force and the buoyant force on a particle at the wall[21], and is defined as

$$\theta = \frac{\tau_w}{2(\rho_s - \rho_f)ga} \qquad (23)$$

The value of the Froude number in Eq.(8) can be determined from the Shields number as

$$Fr = \frac{1}{2\theta(\rho_r - 1)gaH^{-1}} \qquad (24)$$

The grid number in our computations is $1\,024 \times 128 \times 128$, corresponding to the mesh size $h = H/64$. The time step is $0.0002H/u_\tau$. The flow statistics are obtained by averaging the data in the real fluid domain outside the particle boundaries over a period of typically fifty non-dimensional time units after the statistically stationary state is reached.

1.5 *Validation*

Due to lack of benchmark data for the duct flow laden with finite-size particles, we compare our results of the mean and rms velocities in the single-phase case with the previous direct numerical simulations of

Gavrilakis[1] and Pinelli et al.[3] to validate the accuracy of our computations, and it is shown that our results are in good agreement with the previous results.

2. Results and discussions

We will present and discuss our results for the mean secondary flow, the mean streamwise velocity, the RMS velocities, and the distribution of the particle concentration in the following sub-sections.

(a) Velocity vector
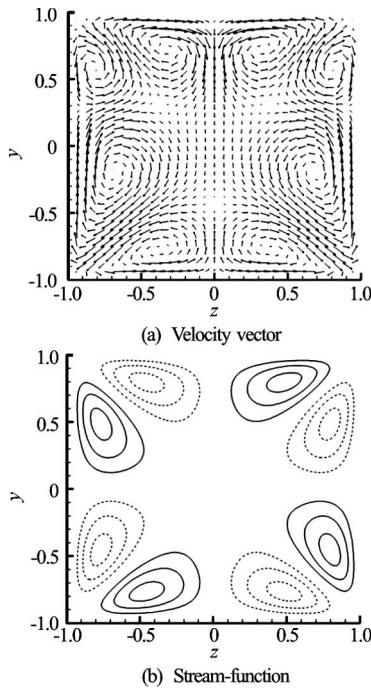
(b) Stream-function

Fig.2 Mean secondary velocity vectors and contours of the corresponding stream-functions $\bar{\psi}(y,z)$ for the single-phase turbulent duct flow. For the contours, the increment is 0.01, and the dashed lines correspond to negative values and continuous lines to positive ones

2.1 Mean secondary motion

The velocity vectors and the stream-function of the mean secondary flow in the single-phase case are shown in Fig.2, in order to make a comparison with the particle-laden flows given below. The flow takes the form of a pair of counter-rotating vortices in each quadrant, transporting the fluid momentum from the bulk region to the corner along the corner bisector. The mean secondary stream-function is determined from the mean streamwise vorticity $\bar{\omega}_x$ by using the following equation

$$\nabla^2 \bar{\psi} = -\bar{\omega}_x \tag{25}$$

The maximum of the stream-function reflects the flow rate in the circulation and thereby the intensity of

the mean secondary flow. The magnitude of the mean secondary velocity is about one percent of that of the bulk velocity, and consequently an accurate computation of the mean secondary flow is a challenging task.
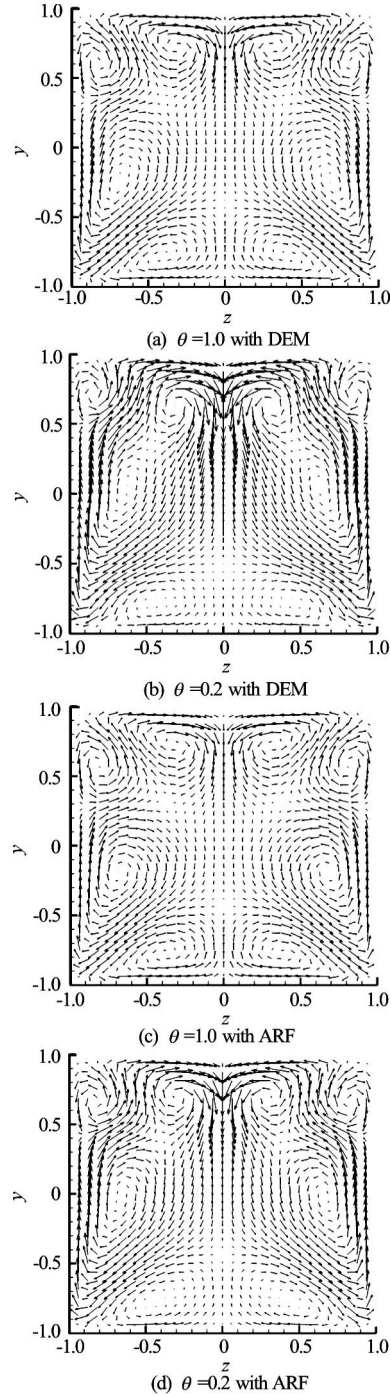

(a) $\theta = 1.0$ with DEM

(b) $\theta = 0.2$ with DEM

(c) $\theta = 1.0$ with ARF

(d) $\theta = 0.2$ with ARF

Fig.3 Mean secondary velocity vectors for different Shields numbers ($\theta = 1.0$ and $\theta = 0.2$) and collision models (DEM and ARF)

Figures 3 and 4 show the velocity vectors and the stream-function of the mean secondary flow for $\theta = 1.0$ and 0.2, respectively. As mentioned earlier, the

Shields number represents the ratio of the shear force to the buoyant force on a particle. The particle settling effect is stronger at a lower Shields number, and at $\theta = 0.2$ most particles settle down to the bottom wall, as shown in Fig.11. Due to the particle sedimentation, the original top-bottom symmetry of the secondary vortices is broken. From the bottom wall to the top wall, the first and the third vortices (i.e., the anti-clockwise rotating vortices with a positive stream-function value in the left half duct) are weakened, and the second and the fourth are enhanced by the particles, as seen in Figs.2, 3 and 4. The second and fourth vortices are connected to each other and appear to merge in the particle-laden cases, resulting in a stronger and larger circulation which transports the fluid downward in the center region and upward along the side walls.
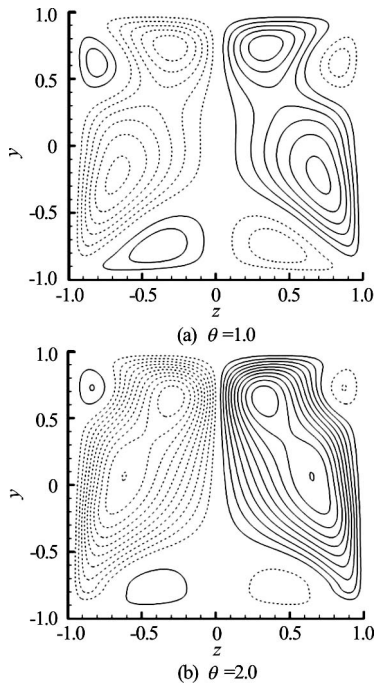

(a) $\theta = 1.0$

(b) $\theta = 2.0$

Fig.4 Contours of the mean stream-functions $\overline{\psi}(y,z)$ for $\theta = 1.0$ and 0.2 with the DEM collision model. The increment for the contours is 0.01

The suppression of the first vortex in the vicinity of the bottom wall is expected to be primarily caused by the hindering effect of the sediments. In Fig.3, the mean secondary flows obtained from ARF and DEM collision models are also compared, in order to examine the effects of the collision model. We see that the suppression of the first vortex is more significant for the DEM model, which is understandable due to the fact that the tangential friction between the particles and the wall in the DEM model hinders the motion of the particles. The effect of the collision model is important, but does not change the results qualitatively.

(a) Nomal stress gradients for particle-free case

(b) Nomal stress gradients for particle-laden case

(c) Nomal stress difference for particle-free case

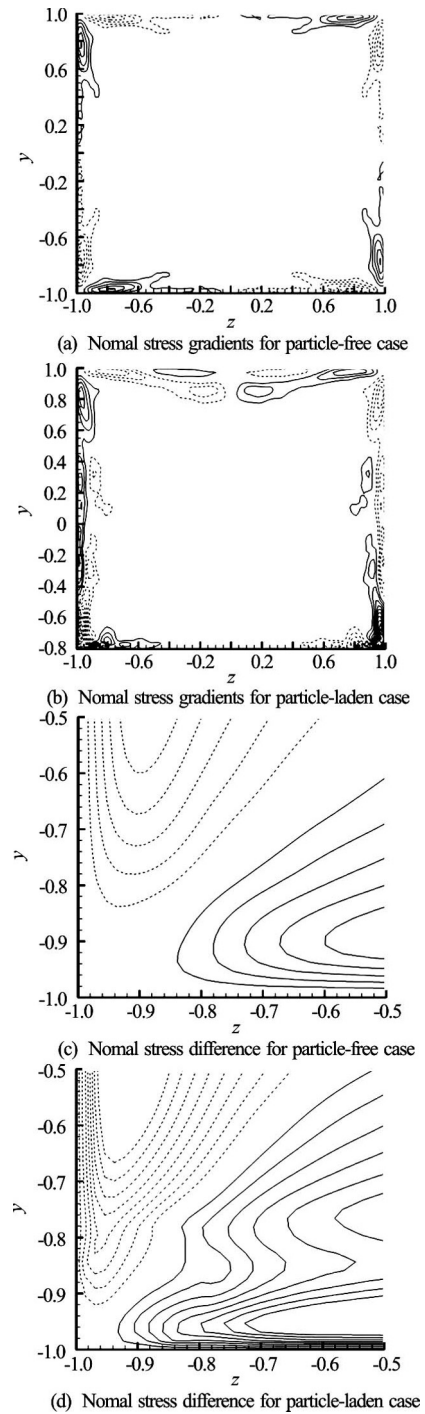(d) Nomal stress difference for particle-laden case

Fig.5 Contours of the normal stress difference gradient term in the mean vorticity equation and the normal stress difference $(\overline{w'^2} - \overline{v'^2})$ for the particle-free case and the particle-laden case at $\theta = 0.2$. The contour increment is 6 for the normal stress difference gradients and 0.1 for the normal stress difference

It seems that there exists a competition between the four vortices. The suppression of the first vortex is expected to be beneficial to the enhancement of the intensity of the second vortex. In addition, the particle

effect may directly enhance the second vortex. In our previous work, it was observed that the particle addition increases the intensity of the mean secondary flow in the neutrally buoyant case and we explained this result by using the mean streamwise vorticity equation. This equation for the fully developed single-phase flow takes a simple form[1] as

$$
\underbrace{\left(\overline{v}\frac{\partial\overline{\omega_x}}{\partial y}+\overline{w}\frac{\partial\overline{\omega_x}}{\partial z}\right)}_{\text{Convection term}}+\underbrace{\left[\frac{\partial^2}{\partial y\partial z}(\overline{w'^2}-\overline{v'^2})\right]}_{\text{Normall stress term}}+
$$

$$
\underbrace{\left[\left(\frac{\partial^2}{\partial y^2}-\frac{\partial^2}{\partial z^2}\right)\overline{v'w'}\right]}_{\text{Shear stress term}}+\underbrace{\left[-\frac{1}{Re_\tau}\left(\frac{\partial^2}{\partial y^2}+\frac{\partial^2}{\partial z^2}\right)\overline{\omega_x}\right]}_{\text{Viscous diffusion term}}=0
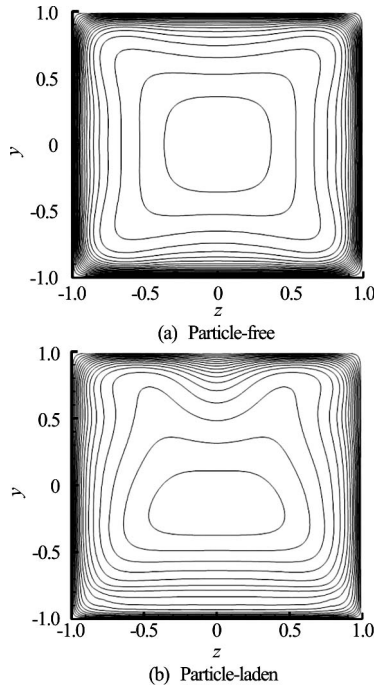$$

$$(26)$$

(a) Particle-free

(b) Particle-laden

Fig.6 Contours of the mean streamwise velocity for the particle-free case and the particle-laden case at $\theta=0.2$. The contour increment is 1

The terms in the first bracket on the left-hand side of Eq.(26) represent the convection of the mean vorticity by the secondary flow itself. The last term represents the viscous diffusion of the mean vorticity. The other two terms are related to the Reynolds stresses due to the Reynolds averaging of the Navier-Stokes equation, generally described as the source of vorticity[1]. The first term is associated with the gradients in the Reynolds cross-stream normal stress difference, and the second term is associated with the
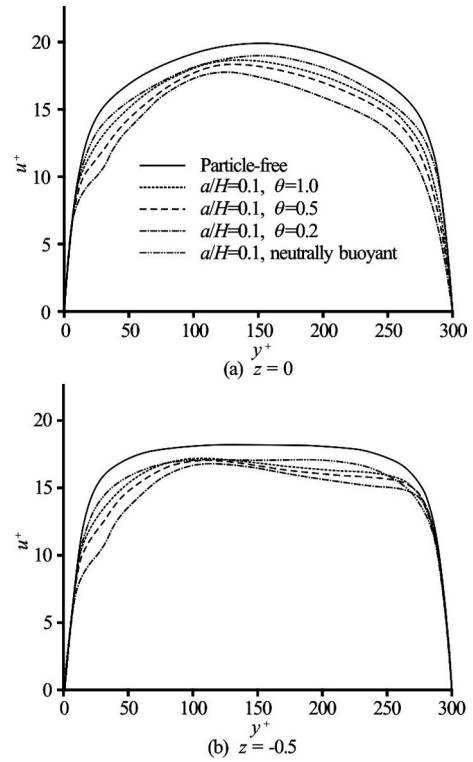

(a) $z=0$

(b) $z=-0.5$

Fig.7 Mean streamwise velocity distributions along a line parallel to the y-axis at $z=0$ and $z=-0.5$, respectively
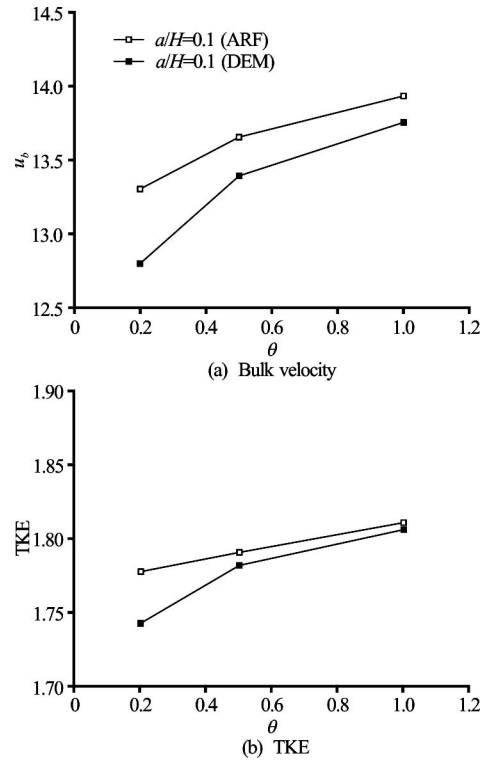

(a) Bulk velocity

(b) TKE

Fig.8 The bulk velocities and mean turbulent kinetic energies as the function of Shields number
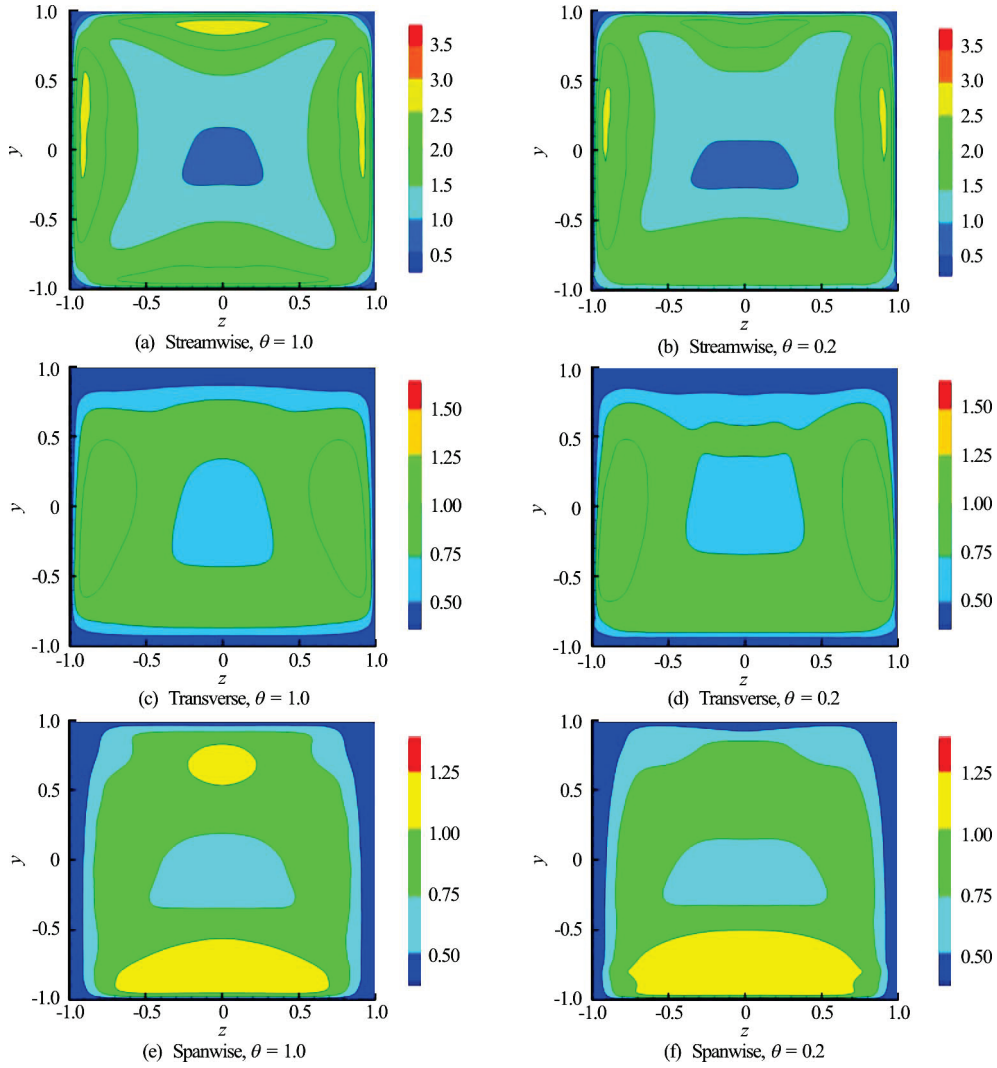
Fig.9 (Color online) Contours of the streamwise, transverse and spanwise rms velocity components for $\theta = 1.0$ and $\theta = 0.2$

Reynolds secondary shear stress. The flow statistics in the particle-laden case in our simulations are defined in the real fluid domain, thus Eq.(26) should hold approximately true for the particle-laden flows at the relatively low particle volume fractions, as indeed evidenced in our previous simulations in the neutrally buoyant case. It was demonstrated that the normal stress term is more important than the shear stress term for the generation of the mean secondary flow. Therefore, we here only plot the distribution of the normal stress difference $(\overline{w'^2} - \overline{v'^2})$ and its gradients in both particle-free and particle-laden cases for the comparison in Fig.5. In the particle-laden case at $\theta = 0.2$, we are only concerned with the flow statistics for $y > -0.8H$, since the region for $y < -0.8H$ are mainly occupied by the particle sediments, in view of the fact that the particle diameter is $0.2H$. The particle-induced enhancement of the gradients of the normal stress difference in the regions where the second and fourth

vortices are located can be observed in Fig.5(b), as compared to Fig.5(a). The enhancement is most pronounced near the side wall at $y = 0.6 - 0.8$. We then compare the normal stress difference in the particle-free and particle-laden cases in Figs.5(c) and 5(d), respectively. The enhancement of the normal stress difference near the side wall at $y = 0.6 - 0.8$ by the particle effect is clear, which explains the enhancement of its gradients.

2.2 Mean streamwise velocity

We now discuss our results of the mean velocity. The contours of the mean streamwise velocity in the particle-free case and the particle-laden case at $\theta = 0.2$ are compared in Fig.6. Although the intensity of the mean secondary flow is smaller by two orders of magnitude than that of the main-stream velocity (i.e., the bulk velocity), it does significantly affect the distribution of the mean streamwise velocity. In the neutrally buoyant case, the mean secondary flow tran-
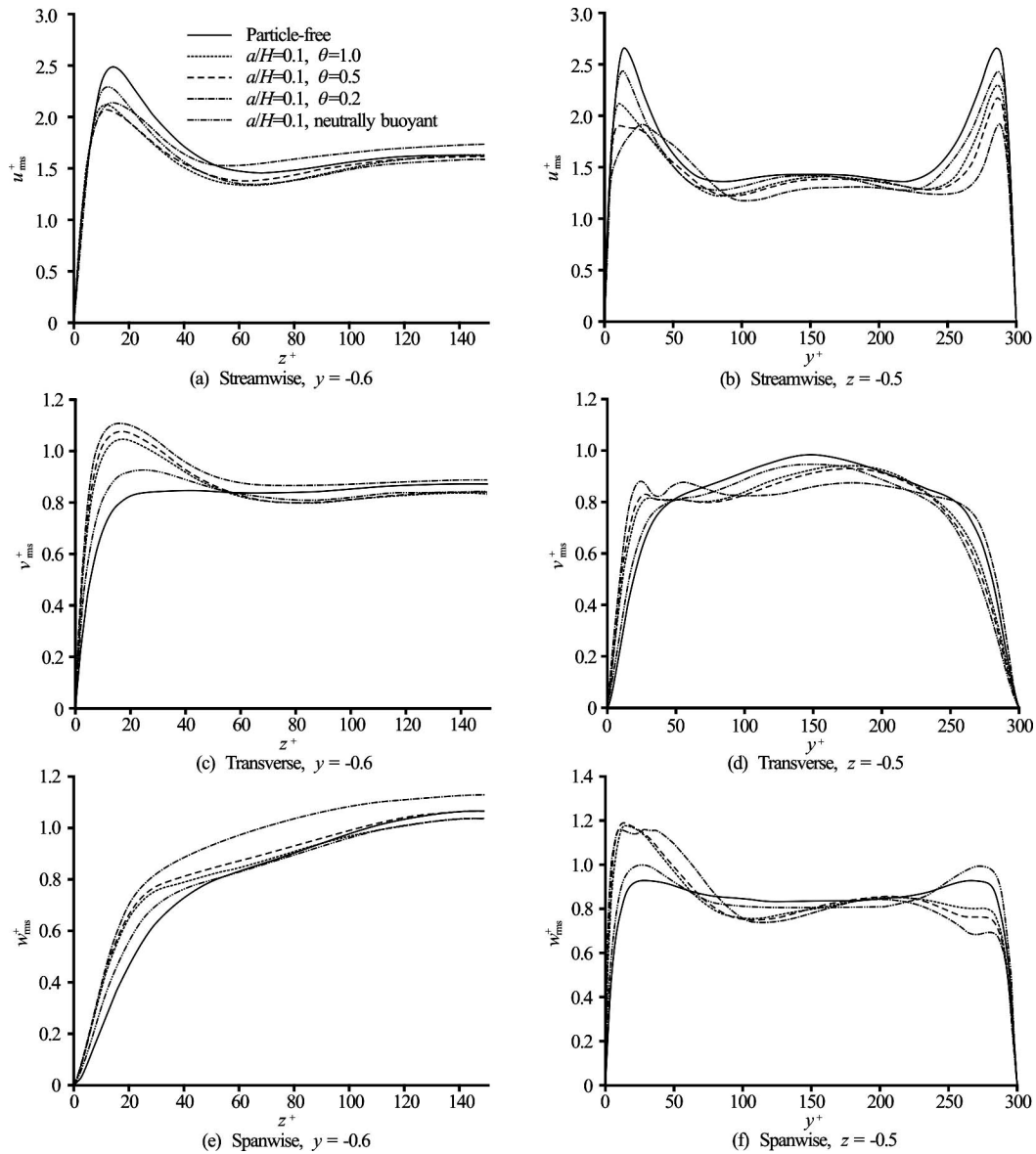
Fig.10 The distributions of the streamwise, transverse and spanwise rms velocity components along a line parallel to the z-axis at $y = -0.6$, and a line parallel to y-axis at $z = -0.5$

sports the high-speed fluids from the bulk region to the corner region, and the low-speed fluids from the wall region to the bulk region along the center-line, resulting in the distortion of the contours of the stream-wise mean velocity in Fig.6(a), namely, with relatively higher streamwise mean velocity along the diagonal line than along the centerline of the cross section at the same y-position (say $y = 0.7$). In the particle-laden case at $\theta = 0.2$, the enhanced secondary circulation due to the second and fourth vortices discussed earlier makes the distribution of the streamwise mean velocity more inhomogeneous along the spanwise direction in the upper half duct, and the significant attenuation of the bottom vortex pair makes the distribution of the mean streamwise velocity more

homogeneous spanwisely in the lower half duct. In addition, it is interesting to note that the maximum streamwise mean velocity occurs in the lower half duct as a result of the mean secondary flow effect (i.e., the mean secondary flow transports the fluids downwards in the center region), in contrast to the observation in the plane channel flow where there is no mean secondary flow and the maximum mean velocity occurs in the upper half channel[11].

The profiles of the streamwise mean velocity at $z = 0$ and $z = -0.5$ for different Shields numbers are shown in Fig.7, which is a complement to Fig.6 and directly shows that the maximum streamwise mean velocity occurs in the lower half duct due to the particle settling effect. In addition, Fig.7 indicates that the

flow rate (or the bulk velocity) is decreased with the decrease of the Shields number, which means that the flow resistance is enhanced as the particle settling effect increases, in view of the fact that the pressure gradient is fixed and the lower flow rate corresponds to the higher flow resistance. Figure 8 shows the bulk velocity as a function of the Shields number for two collision models, and the results again indicate that the effect of the collision model is significant (the relative difference in the bulk velocity at $\theta = 0.2$ is around 4%), but does not change the results qualitatively. The higher flow resistance for the DEM collision model can be explained by the fact that the friction between the particles and the wall is considered for the DEM model.

2.3 rms velocities

We have discussed the role of the Reynolds normal stress difference in the generation of the mean secondary flow. The Reynolds normal stress component is actually the rms velocity. Now we inspect the effects of the particles on the rms velocity components. Figure 9 shows the contours of three rms velocity components for $\theta = 1.0$ and 0.2, respectively, with an overview of the rms velocity distribution. As the Shields number is decreased from 1.0 to 0.2, the streamwise rms velocity becomes smaller in most regions, whereas the transverse and spanwise rms velocities are, roughly speaking, enhanced in the lower half duct and weakened in the upper half duct. Figure 10 shows the distribution of the rms velocity components along a line parallel to the z-axis at $y = -0.6$, and a line parallel to y-axis at $z = -0.5$, which further supports the above observation. One reason for the overall decrease of the streamwise rms velocity at a lower Shields number is that the bulk velocity decreases with the decrease of the Shields number. The further decrease of the streamwise mean velocity near the top wall (see Fig.7(a)) due to the effect of the mean secondary flow is responsible for the pronounced attenuation of the streamwise rms velocity near the top wall, and the effect of the particle sediments results in the attenuation of the streamwise rms velocity near the bottom wall (from the comparison between Figs.9(a) and 9(b)). The particle-induced vortices (or vortex shedding) give rise to the enhancement of the transverse and spanwise rms velocity components near the wall. Along the line of $y = -0.6$, the particle-induced enhancement of the wall-tangential rms velocity (v_{rms}) is larger than that in the wall-normal rms velocity (w_{rms}) in the near-wall region, which explains the enhancement of the magnitude of the normal stress difference $(\overline{w'^2} - \overline{v'^2})$, observed earlier.

Shao et al.[11] investigated numerically the effects of the settling particles on the turbulent channel flow at a constant flow rate, and observed that the particle sediments increased significantly the rms velocities in the bulk region due to the vortex-shedding from the particles. In contrast, the present simulations show that the turbulence intensity is reduced when the particle settling effect is increased, as shown in Fig.8(b). The primary reason for the discrepancy may be that in the present study the pressure gradient is fixed and the flow rate decreases with the decrease of the Shields number, whereas the flow rate is fixed in Shao et al.[11].

2.4 Particle distribution

It is shown that in the neutrally buoyant case the particle concentration is higher in the near-corner region. The distributions of the particle concentration (or the local volume fraction) for $\theta = 1.0$ and 0.2 are shown in Fig.11. One can see that the particle concentration is higher at the face center of the bottom wall, which is clearly caused by the mean secondary flow. For $\theta = 0.2$, most particles settle down to the bottom wall and form one layer of particle sediments, and the particle can be trapped in the corner for a long time once it is bumped there due to the interaction with other particles, resulting in a high particle concentration there.
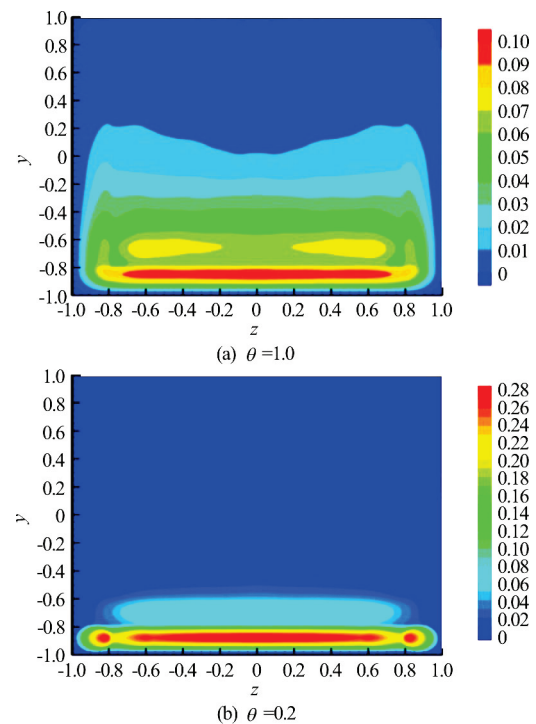

(a) $\theta = 1.0$

(b) $\theta = 0.2$

Fig.11 (Color online) The spatial concentration distributions of the particles in the cross section for $\theta = 1.0$ and $\theta = 0.2$

3. Conclusions

The particle-laden turbulent flows in a square

duct are numerically simulated with a parallel direct-forcing fictitious domain method. The effects of finite-size heavy particles on the mean secondary flow, the mean streamwise velocity, the root-mean-square of the velocity fluctuation, and the particle concentration distribution are investigated at the friction Reynolds number of 150, the particle volume fraction of 2.36%, the particle diameter of 0.1 duct width, and the Shields number ranging from 1.0 to 0.2. From our results, the following conclusions can be drawn:

(1) The particle sedimentation breaks the up-down symmetry of the mean secondary vortices, and results in a stronger circulation which transports the fluids downward in the bulk center region and upward along side walls at a low Shields number. This circulation has a significant impact on the distribution of the mean streamwise velocity, whose maximum value occurs in the lower half duct, unlike the plane channel case.

(2) The flow resistance is increased and the turbulence intensity is reduced, as the Shields number is decreased.

(3) As the Shields number is decreased, the streamwise rms velocity becomes smaller in most regions, whereas the transverse and spanwise rms velocities are, roughly speaking, enhanced in the lower half duct and weakened in the upper half duct. Along the line of $y = -0.6$, the particle-induced enhancement of the wall-tangential rms velocity (v_{rms}) is larger than that in the wall-normal rms velocity (w_{rms}) in the near-wall region, resulting in the enhancement of the magnitude of the normal stress difference term there, which might be one reason for the enhancement of the second mean secondary vortex from the bottom wall.

(4) The particles accumulate preferentially at the face center of the bottom wall, due to the effect of the mean secondary flow.

(5) The collision model has an important quantitative effect on the results, but does not change the results qualitatively.

References

[1] Gavrilakis S. Numerical simulation of low-Reynolds-number turbulent flow through a straight square duct [J]. *Journal of Fluid Mechanics*, 1992, 244: 101-129.

[2] Uhlmann M., Pinelli A., Kawahara G. et al. Marginally turbulent flow in a square duct [J]. *Journal of Fluid Mechanics*, 2007, 588: 153-162.

[3] Pinelli A., Uhlmann M., Sekimoto A. et al. Reynolds number dependence of mean flow structure in square duct turbulence [J]. *Journal of Fluid Mechanics*, 2010, 644: 107-122.

[4] Winkler C. M., Rani S. L., Vanka S. P. Preferential concentration of particles in a fully developed turbulent square duct flow [J]. *International Journal of Multiphase Flow*, 2004, 30(1): 27-50.

[5] Sharma G., Phares D. J. Turbulent transport of particles in a straight square duct [J]. *International journal of multiphase flow*, 2006, 32(7): 823-837.

[6] Winkler C. M., Rani S. L., Vanka S. P. A numerical study of particle wall-deposition in a turbulent square duct flow [J]. *Powder Technology*, 2006, 170(1): 12-25.

[7] Yao J., Fairweather M. Particle deposition in turbulent duct flows [J]. *Chemical Engineering Science*, 2012, 84: 781-800.

[8] Yao J., Fairweather M., Zhao Y. L. Numerical simulation of particle deposition in turbulent duct flows [J]. *Industrial and Engineering Chemistry Research*, 2014, 53(8): 3329-3341.

[9] Yao J., Fairweather M. Inertial particle resuspension in a turbulent, square duct flow [J]. *Physics of Fluids*, 2010, 22(3): 033303.

[10] Wu T. H., Shao X. M., Yu Z. S. Fully resolved numerical simulation of turbulent pipe flows laden with large neutrally-buoyant particles [J]. *Journal of Hydrodynamics*, 2011, 23(1): 21-25.

[11] Shao X., Wu T., Yu Z. Fully resolved numerical simulation of particle-laden turbulent flow in a horizontal channel at a low Reynolds number [J]. *Journal of Fluid Mechanics*, 2012, 693: 319-344.

[12] Kidanemariam A. G., Chan-Braun C., Doychev T. et al. Direct numerical simulation of horizontal open channel flow with finite-size, heavy particles at low solid volume fraction [J]. *New Journal of Physics*, 2013, 15(2): 025031.

[13] Do-Quang M., Amberg G., Brethouwer G. et al. Simulation of finite-size fibers in turbulent channel flows [J]. *Physical Review E*, 2014, 89(1): 013006.

[14] Picano F., Breugem W. P., Brandt L. Turbulent channel flow of dense suspensions of neutrally buoyant spheres [J]. *Journal of Fluid Mechanics*, 2015, 764: 463-487.

[15] Wang L. P., Peng C., Guo Z. et al. Flow modulation by finite-size neutrally buoyant particles in a turbulent channel flow [J]. *Journal of Fluids Engineering*, 2016,138(4): 041306.

[16] Glowinski R., Pan T. W., Hesla T. I. et al. A distributed Lagrange multiplier/fictitious domain method for particulate flows [J]. *International Journal of Multiphase Flow*, 1999, 25(5): 755-794.

[17] Yu Z., Shao X. A direct-forcing fictitious domain method for particulate flows [J]. *Journal of Computational Physics*, 2007,227(1): 292-314.

[18] Shao X. M., Zhang X. L., Yu Z. S. Numerical studies of the hysteresis in locomotion of a passively pitching foil [J]. *Journal of Hydrodynamics*, 2016, 28(3): 359-368.

[19] Zhang H. Z., Yu Z. S., Shao X. M. Numerical study on the propulsion of a biomimetic jellyfish [J]. *Chinese Journal of Hydrodynamics*, 2016, 31(3): 327-333(in Chinese).

[20] Crowe C. T., Schwarzkopf J. D., Sommerfeld M. et al. Multiphase flows with droplets and particles [M]. Boca Raton, USA: CRC Press, 2011, 124-132.

[21] Peysson Y., Ouriemi M., Medale M. et al. Threshold for sediment erosion in pipe flow [J]. *International Journal of Multiphase Flow*, 2009, 35(6): 597-600.